Electronic Supplementary Material (ESI) for Energy & Environmental Science.

Supporting information

Oxygen-vacancy-rich nickel hydroxide nanosheet: a multifunctional layer between Ir and Si toward enhanced solar hydrogen production in alkaline media

Junxia Shen, [a] Ronglei Fan, *[a] Yongjie Wang, [b] Ju Zhou, [a] Cong Chen, [a] Zhihe Wei, [ac] Sheng Ju, *[a] Tao Qian, [d] Yang Peng [c] and Mingrong Shen *[a]

a. School of Physical Science and Technology, Jiangsu Key Laboratory of Thin Films Collaborative Innovation Center of Suzhou Nano Science and Technology Soochow University Suzhou 215006, China. E-mail: rlfan@suda.edu.cn; jusheng@suda.edu.cn; mrshen@suda.edu.cn;

b. School of Science, Harbin Institute of Technology, Shenzhen, Shenzhen, 518000, China

c. Soochow Institute of Energy and Material Innovations, College of Energy, Provincial Key Laboratory for Advanced Carbon Materials and Wearable Energy Technologies, Soochow University, Suzhou 215006, China

d. School of Chemistry and Chemical Engineering, Nantong University, Nantong 226000, China

Experimental Section

Materials and methods

Nickel dichloride hexahydrate ($NiCl_2·6H_2O$), sodium chloride (NaCl), Iridium tetrachloride tetrahydrate ($IrCl_4·4H_2O$), Sodium borohydride ($NaBH_4$), and sodium hydroxide (KOH) were used as received. All reagents were of analytical grade and used without further purification. Deionized water with a resistivity of about 18.5 MΩ was used throughout the experimental processes.

Fabrication of n^+np^+-Si with micro-pyramid textured surfaces

Single-crystalline n-type Si (100) wafers (156×156×0.18 mm^3,1–3 Ω•cm specific resistance, Canadian Solar Inc.) were used for this work. The pyramid surface texture on both sides of silicon wafers was produced by chemical etching in a solution of KOH on a mass production line of crystalline-Si solar cells in the Suzhou company of Canadian Solar Inc. To form an n^+ emitter layer and a p^+ electron back reflection layer for the n-Si, the as prepared n-Si wafers were first coated with liquid phosphorus and boron doped precursors respectively, subsequently, a thermal diffusion process was conducted at 950 °C for 180 min under the atmosphere of nitrogen in a diffusion furnace. After doping, an anti-reflection SiN_x layer and fritted Ag bare line were produced onto the p^+-Si emitter side. Finally, the samples were laser-cut into 1.5×1.5 cm^2. We denote such a sample as Si. Before use, Si electrodes were cleaned by subsequent sonication in acetone, ethanol and water for 5 minutes each to remove any contaminants, and dried under a stream of N_2.

E-beam evaporation of the Ni film

Before the metal deposition, The native SiO_2 layer on the n^+ side was then etched by dropping 5 wt % HF solution. A Ni layer was deposited on the Si surface via E-beam evaporation at a deposition rate of 0.5 Å/s. A layer thickness of ~12 nm was controlled and measured by using the transmission electron microscopy (TEM).

Fabrication of Ni/Si photocathode

In order to form an ohmic contact between the copper wire and both sides of Si, tinned Cu wire was embedded by Ag paste and then glued to the Ag bar on anti-reflection SiN_x layer (W1 for the photoelectrochemical test) and the Ni surface (W2, for electrochemical measurement). After the Ag paste is dried completely, a quartz plate (1.5×1.5 cm^2) was adhered to the SiN_x side. At last, edges and some part of the front surface of the electrodes (except for the intended reaction area 1×1 cm^2) were sealed with an industrial epoxy (PKM12C-1, Pattex).

Synthesis of $Ni(OH)_2$ and r-$Ni(OH)_2$ onto the Ni/Si photocathodes

$Ni(OH)_2$ layer was synthesized on Ni/Si photocathode through an atmospheric solvothermal reaction in a an aqueous solution. 20 mM $NiCl_2$ and 0.5 M NaCl were dissolved in deionized water in a beaker to form a homogeneous precursor solution. The above beaker was transferred to a water bath kettle with a temperature of 90℃ and stirred with a frequency of 200 rpm/min. Then, a piece of Ni/Si photocathode was hung on the edge of the beaker and immersed in the precursor solution for 6 h to obtain the $Ni(OH)_2$/Ni/Si photocathode. Finally, r-$Ni(OH)_2$/Ni/Si photocathode was synthesized by treating $Ni(OH)_2$/Ni/Si with $NaBH_4$ (0.25 mmol) for various times (t=5, 20, 60 and 180 s). The achieved $Ni(OH)_2$/Ni/Si and r-$Ni(OH)_2$/Ni/Si photocathodes were washed with ethanol and deionized water three times and dried under atmospheric pressure in an oven at 60℃ overnight.

Deposition of Ir catalyst onto the Ni/Si, $Ni(OH)_2$/Ni/Si and r-$Ni(OH)_2$/Ni/Si photocathodes

The deposition of Ir catalyst onto the various photocathodes was carried out in an electrodeposition bath with a three-electrode cell configuration, using the W1 as the working electrode, Ag/AgCl (3 M KCl) as the reference electrode, and a Ni wire as the counter electrode. The electrodeposition bath consists of an aqueous solution of different amounts of $IrCl_4 \cdot xH_2O$ and 1 M KOH. The precursor solution was purged with nitrogen for 30 min before deposition. The electrodeposition of the Ir catalyst onto the surface of various electrodes was performed by cyclic voltammetry between 0.1 and -0.4 V_{RHE} for various cycles under simulated AM 1.5G one sun illumination. Then, the Ir/Ni/Si, Ir/$Ni(OH)_2$/Ni/Si and Ir/r-$Ni(OH)_2$/Ni/Si photocathodes were obtained. The electrode was again rinsed with copious water gently and dried with a stream of nitrogen.

Materials characterization

The surface morphology of the sample was analyzed using a field-emission scanning electron microscope (SEM) (SU8010, Hitachi). Transmission electron microscope (TEM) and EDX elemental maps analysis was conducted by a Tecnai G220 (S-TWIN, FEI) operating at 200 kV. X-ray diffraction (XRD) was measured using an X-ray diffractometer in parallel beam mode with Cu K_α radiation (D/MAX-2000PC, Japanese Rigaku). Raman spectra of the samples were measured by Raman spectroscopy (Horiba JY LabRAM HR800, λ=532nm). The oxygen vacancies of samples were measured by electron paramagnetic resonance (EPR) (Bruker A300, Germany). X-ray photoelectron spectroscopy (XPS) measurements were performed at room temperature using a spectrometer hemispherical analyzer (ESCALAB 250Xi, Thermo). All the binding energies were referenced to adventitious carbon at 284.6 eV. Elemental analysis of metal ions was determined by Inductively Coupled Plasma-Atomic Emission Spectrometry (ICP-AES) with an OPTIMA 8000 analyzer (PerkinElmer Inc).

Photoelectrochemical (PEC) and Electrochemical (EC) measurements

A solar simulator (Newport Oriel) with an AM 1.5G filter was used as the light source. Before the PEC measurement, the light intensity was carefully controlled at 100 mW cm^{-2}, measured using an optical power meter (Newport Company) just before the light enters into the PEC cell. The PEC and EC measurements including LSV, EIS, CV and J–t tests were performed using an electrochemical workstation (SP-200, Bio-Logic) in a solution containing 1 M KOH (pH=13.6). The final potential was translated into the

RHE according to the following equation: $\mathrm{V_{RHE}} = \mathrm{V_{Ag/AgCl}} + 0.059 \times \mathrm{pH}$, where $\mathrm{V_{Ag/AgCl}} = 0.197\ \mathrm{V}$.

The PEC performance of the Si photocathodes was conducted in a three-electrode configuration with the W1 of Si photoelectrode as the working electrode, an Ag/AgCl (3 M KCl) as the reference electrode and a Ni wire as the counter electrode. Similarly, the electrochemical activity of various catalysts was also conducted in a three-electrode configuration using, with the W2 of Si photoelectrode as the working electrode. LSV measurements were performed at room temperature, with a scan rate of 10 mV/s. The Tafel slopes of different samples stemmed from their corresponding LSV curves. The Tafel slope can be calculated by the Tafel equation: $V_{\mathrm{op}} = a + \mathrm{b} \log (J)$, where J, V_{op}, and b represent the current density, overpotential, and Tafel slope, respectively. C_{dl} can be calculated according to the following equation: $\Delta J = C_{dl} \times v$. The capacitive current ΔJ is plotted as a function of the scan rate v to obtain the C_{dl} values, where ΔJ of the various electrocatalysts are collected at different scan rates, according to the following equation: $\Delta J = (J_a - J_c)/2$, where J_a and J_c are the anodic and cathodic current densities at 0.05 $\mathrm{V_{RHE}}$, respectively. The ECSA is calculated based on $\mathrm{ECSA} = \mathrm{C}_{dl}/\mathrm{C}_s$, where C_s is the specific capacitance and is considered to be a constant, which is reported to be between 0.022 and 0.130 $\mathrm{mF/cm^2}$ in an alkaline solution. In this study, we assumed the value of C_s to be 0.040 $\mathrm{mF/cm^2}$. The active surface site density and per-site turnover frequency (TOF) for the catalyst is calculated by the following equation: $\mathrm{TOF} = \mathrm{I}/2\mathrm{nF}$, where I is the current (A) during LSV, F is the Faraday constant (96485.3 C/mol), n is the number of active sites (mol). The factor of $1/2$ is based on the assumption that two electrons are necessary to form a hydrogen molecule. The electrochemical impedance spectroscope (EIS) measurements were performed at a constant -0.2 $\mathrm{V_{RHE}}$ in the frequency range from 0.1 Hz to 100 kHz under simulated AM 1.5G one sun illumination. The Faradic efficiency is defined as the ratio of the amount of H_2 evolved during the experiments to the amount of H_2 expected based on theoretical considerations. The evolved H_2 gas during the experiments is collected by water drainage method and the purity of the generated gas was confirmed by gas chromatography (GC) analysis. The moles of H_2 generated from the reaction is calculated with an ideal gas law. To evaluate the stability of different electrodes, long-term J–t measurements were conducted at constant potential 0 V_{RHE} in 1.0 M KOH solution under simulated AM 1.5G one sun illumination. The electrolyte was replaced and the sample was rinsed every 12 h during the stability measurements.

The wetting ability of surface of $Ni(OH)_2$、r-$Ni(OH)_2$、Ir/$Ni(OH)_2$ and Ir/r-$Ni(OH)_2$ photocathodes was characterized by surveying the contact angles of electrolyte, 1 M KOH solution. In the typical measurements, a 4 μL droplet of 1 M KOH solution was dropped on the surface of the electrode and the contact angle was measured by JC2000DM system at room temperature. Each contact angle measurement was repeated more than 3 times. The images of hydrogen bubbles release were obtained by a high-speed digital camera system.

Computational details

The first-principle calculations were performed using the Vienna ab initio simulation package (VASP).[1, 2] The projector augmented wave (PAW) with plane wave cutoff of 400 eV was used to describe the interaction between the atomic cores and electrons.[3] The Generalized Gradient Approximation (GGA) with the Perdew-Burke-Ernzerhof (PBE) exchange-correlation functional was used to describe the semi-local exchange and correlation energies.[4] Meanwhile, the DFT-D2 correction was used to consider the van der Waals interaction. To concentrate on the chemistry of the edges of $Ni(OH)_2$, the semi-infinite ribbon model containing nine Ni atoms with three Ni atoms in the x-direction and y-direction respectively was built. The ribbons were separated by vacuum from each other by 14 Å along the z-axis and 9 Å along the y-direction. A Monkhorst-Pack grid of $3 \times 1 \times 1$ size was used to sample the Brillouin zone in calculations. Structures were relaxed until the total forces were less than 0.02 eV/Å and the convergence criterion for total energies was set to 10^{-5} eV. To better describe the system, we carried out a spin-polarized calculation with a Hubbard-U correction of 3 eV for Ni. The Gibbs free energy change ΔG in hydrogen evolution reaction (HER) were evaluated by the formula: $\Delta \mathrm{G} = \Delta \mathrm{E} + \Delta \mathrm{E}_{\mathrm{ZPE}} - \mathrm{T}\Delta \mathrm{S}$, where $\Delta \mathrm{E}$ represents the adsorption energy of HER intermediates, $\Delta \mathrm{E}_{\mathrm{ZPE}}$ represents the corresponding zero-point energy and $\mathrm{T}\Delta \mathrm{S}$ is the entropy change in each reaction step.[5]

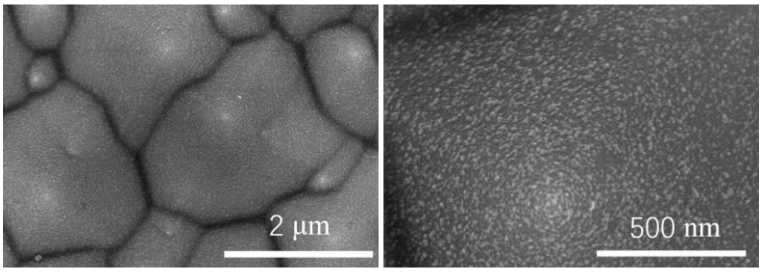

Figure S1. Top-view SEM images of Ir/Ni/Si.

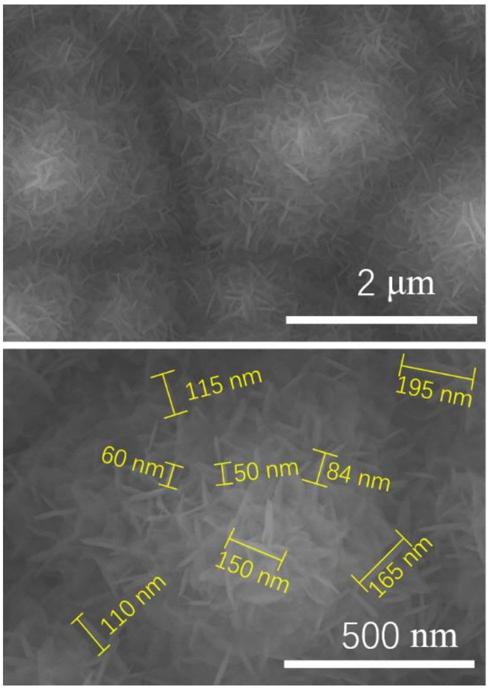

Figure S2. Top-view SEM images of $Ni(OH)_2$/Ni/Si.

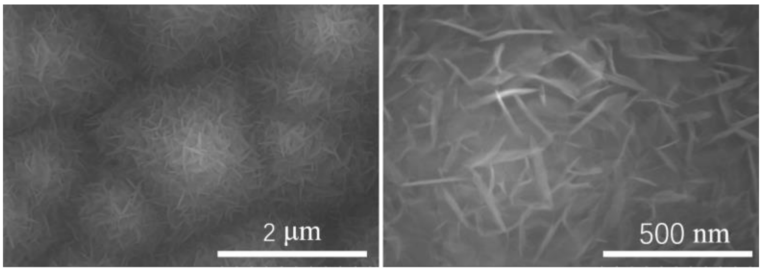

Figure S3. Top-view SEM images of r-$Ni(OH)_2$/Ni/Si.

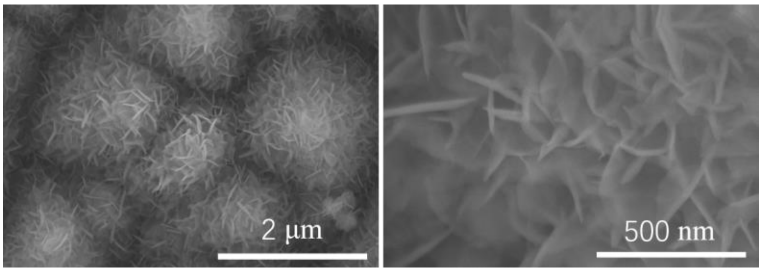

Figure S4. Top-view SEM images of Ir/$Ni(OH)_2$/Ni/Si.

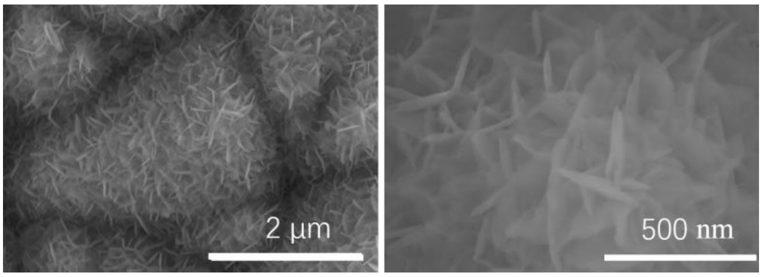

Figure S5. Top-view SEM images of (a, b) Ir/r-$Ni(OH)_2$/Ni/Si.

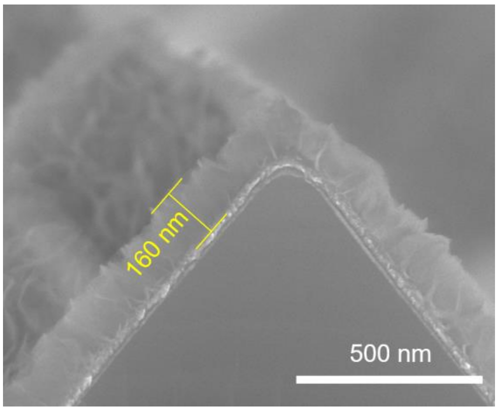

Figure S6. The cross-sectional SEM image of Ir/r-$Ni(OH)_2$.

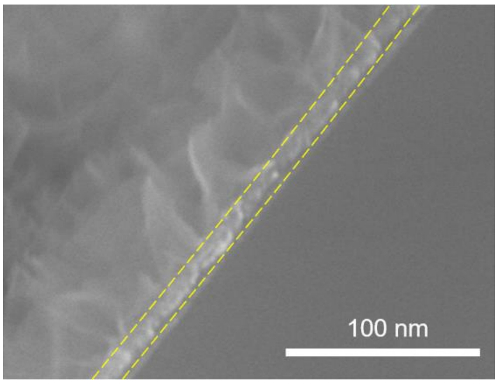

Figure S7. High-resolution cross-sectional SEM images of the Ir/r-Ni(OH)$_2$/Ni/Si.

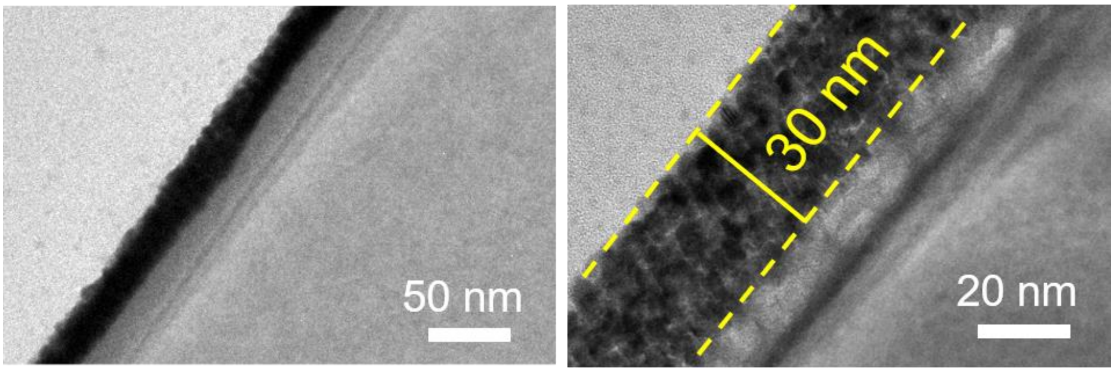

Figure S8. Cross-sectional images of a 30 nm Ni layer deposited on the Si before the growth of Ni(OH)$_2$ layer.

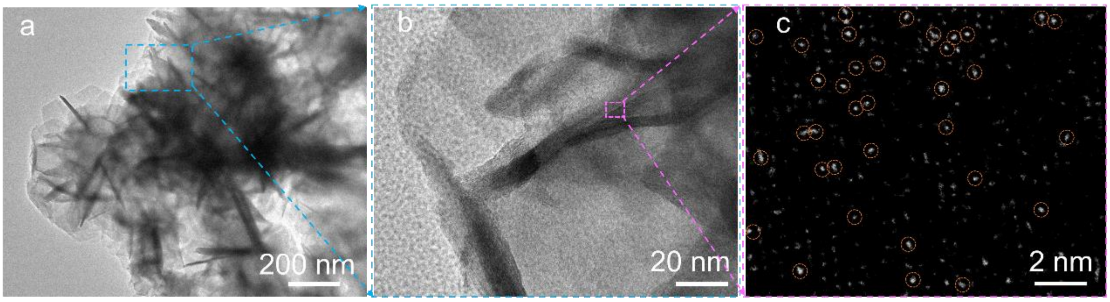

Figure S9. HAADF-STEM image of the Ir/r-Ni(OH)$_2$. Singly dispersed Ir atoms are indicated by yellow circles.

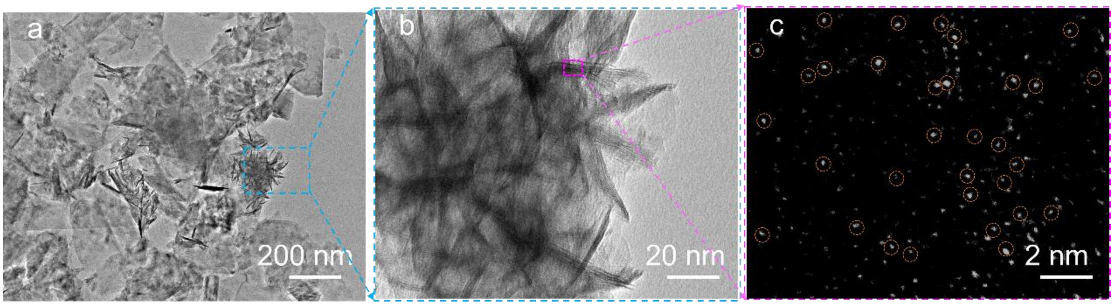

Figure S10. HAADF-STEM image of the Ir/Ni(OH)$_2$. Singly dispersed Ir atoms are indicated by yellow circles.

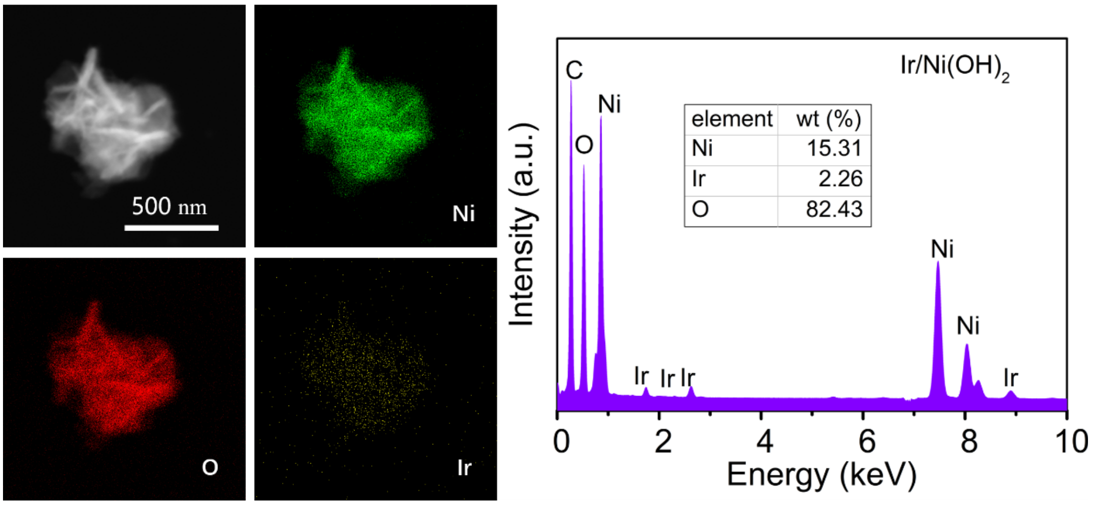

element	wt (%)
Ni	15.31
Ir	2.26
O	82.43

Figure S11. EDX mapping images of Ni, O and Ir elements of the synthesized Ir/Ni(OH)$_2$.

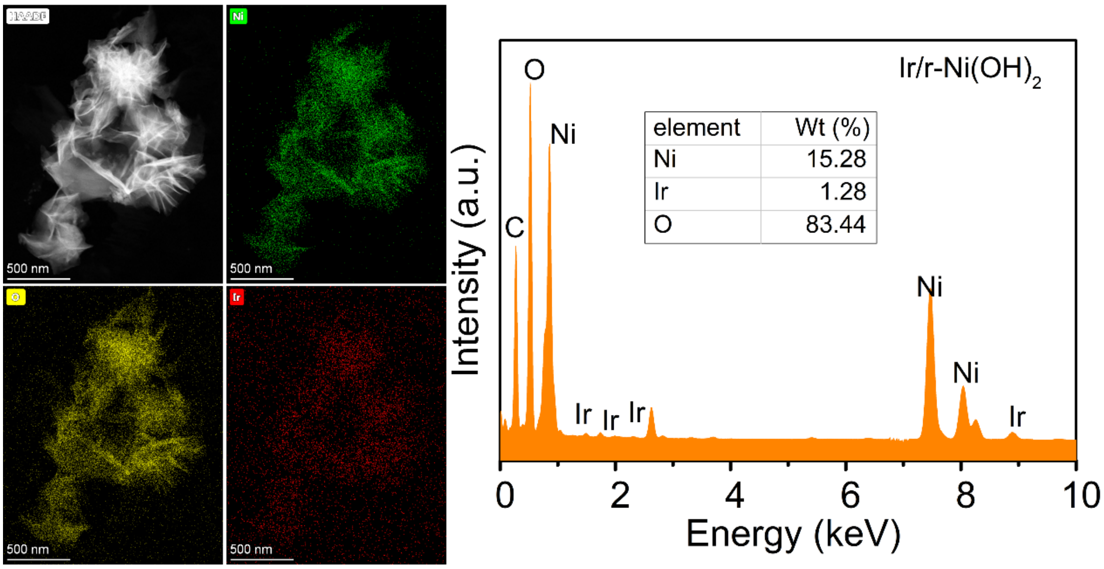

Figure S12. EDX mapping images of Ni, O and Ir elements of the synthesized Ir/r-Ni(OH)$_2$.

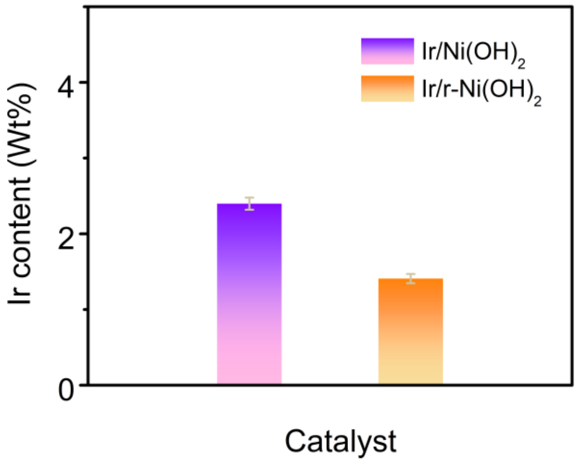

Figure S13. Comparison of Ir content of different samples measured by ICP-AES.

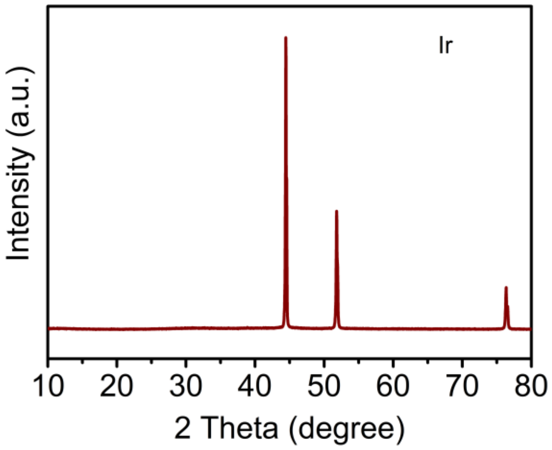

Figure S14. XRD pattern of Ir catalyst on Ni support.

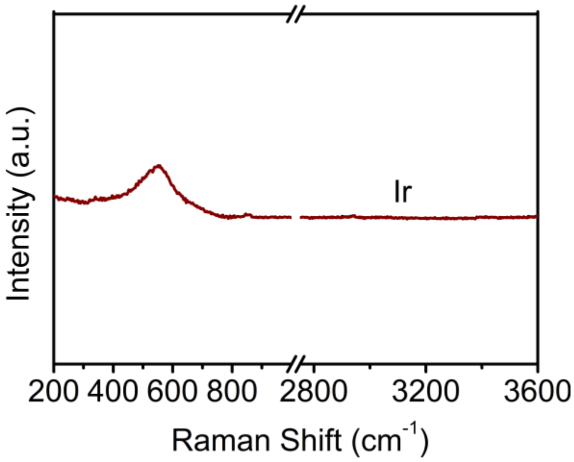

Figure S15. Raman spectum of Ir catalyst on Ni support.

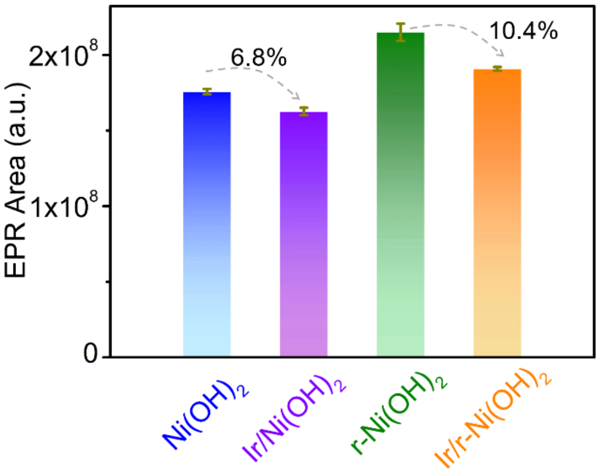

Figure S16. EPR areas of Ni(OH)$_2$, r-Ni(OH)$_2$, Ir/Ni(OH)$_2$ and Ir/r-Ni(OH)$_2$. The EPR area was obtained by a double numerical integration of the first derivative experimental spectrum.

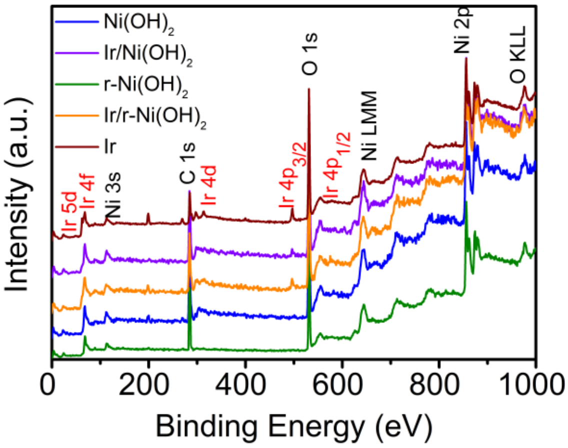

Figure S17. XPS survey spectra of various samples.

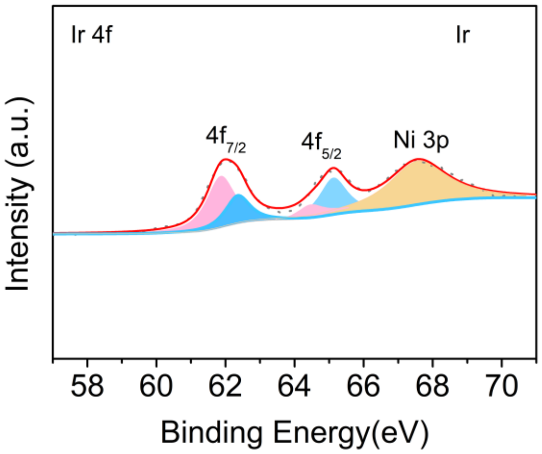

Figure S18. Ir 4f spectra of Ir catalyst on Ni/Si electrode.

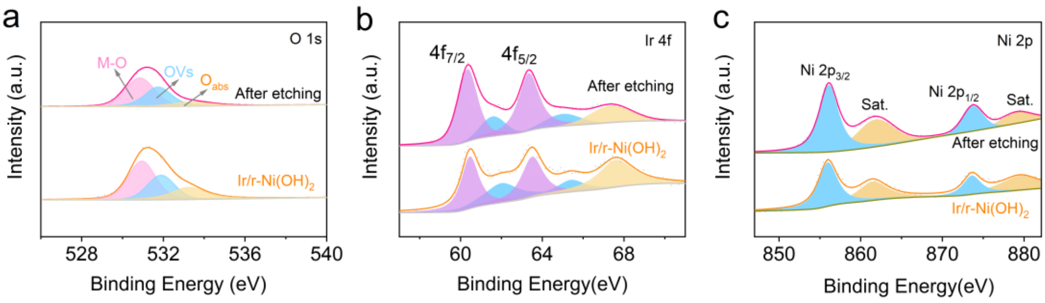

Figure S19. The comparison of high-resolution XPS (a) O 1s, (b) Ir 4f and (c) Ni 2p spectra of the Ir/r-$Ni(OH)_2$ before and after Ar ion etching for 30 s in vacuum. Fig. S19 compares the high-resolution XPS O 1s, Ni 2p and Ir 4f spectra of the Ir/r-$Ni(OH)_2$ before and after Ar ion etching for 30 s in vacuum. In the O 1s region, upon Ar ion etching, the relative peak area of O_{abs} is significantly reduced, while the changes of M−O and OVs components are negligible. Furthermore, the Ni 2p and Ir 4f spectra exhibit very similar features after Ar ion etching in vacuum. Based on above results, we can infer that the adsorbed oxygen on surface after exposure to the atmosphere has no noticeable effect on the oxidation states of sample.

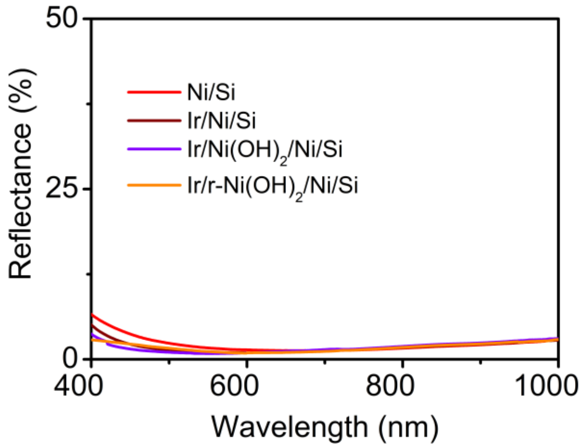

Figure S20. UV-Vis reflectance spectra of Ni/Si, Ir/Ni/Si, Ir/$Ni(OH)_2$/Ni/Si and Ir/r-$Ni(OH)_2$/Ni/Si measured from the rear p^+-Si side under identical conditions.

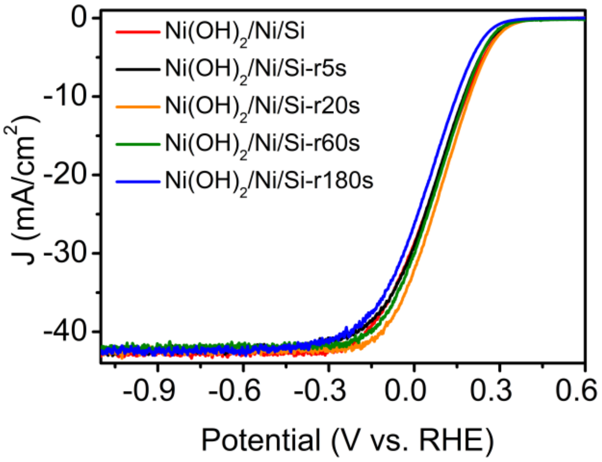

Figure S21. PEC LSV polarization curves of $Ni(OH)_2$/Ni/Si samples treated by $NaBH_4$ for different times under simulated AM1.5G one sun illumination.

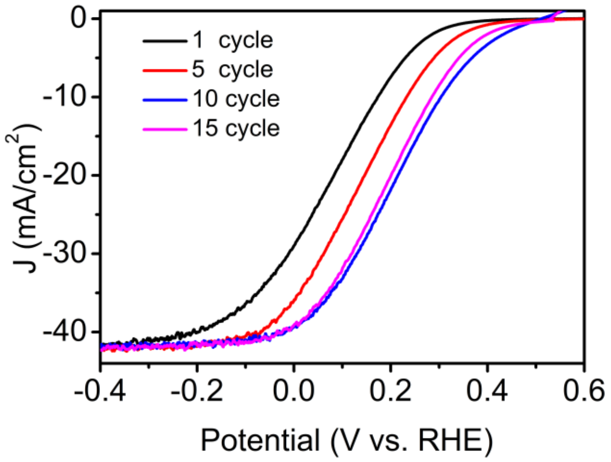

Figure S22. PEC LSV curves of the Ir catalyst with different loading amount on Ni/Si photocathode in 1 M KOH under simulated AM1.5G one sun illumination.

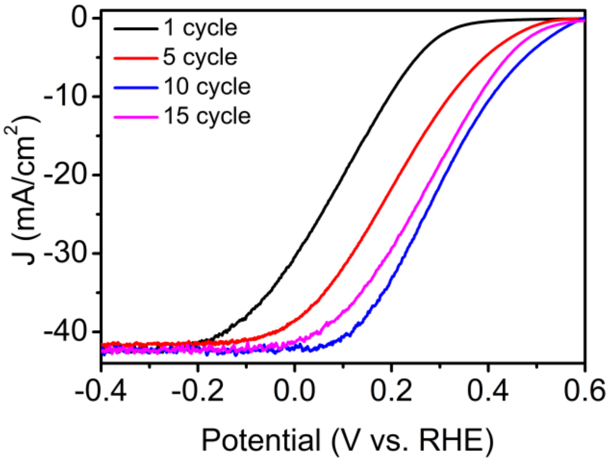

Figure S23. PEC LSV curves of the Ir catalyst with different loading amount on Ni(OH)$_2$/Ni/Si photocathode in 1 M KOH under simulated AM1.5G one sun illumination.

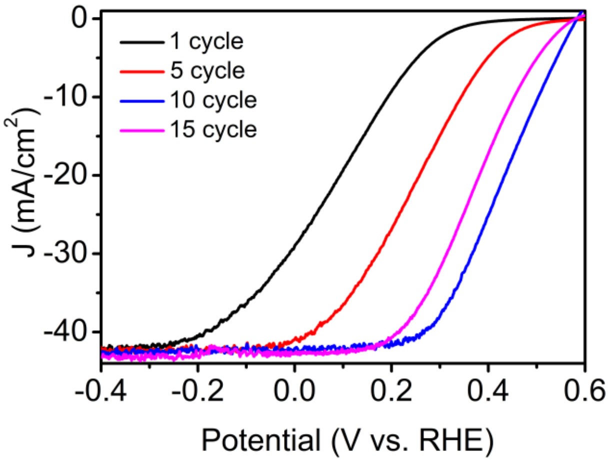

Figure S24. PEC LSV curves of the Ir catalyst with different loading amount on r-Ni(OH)$_2$/Ni/Si photocathode in 1 M KOH under simulated AM1.5G one sun illumination.

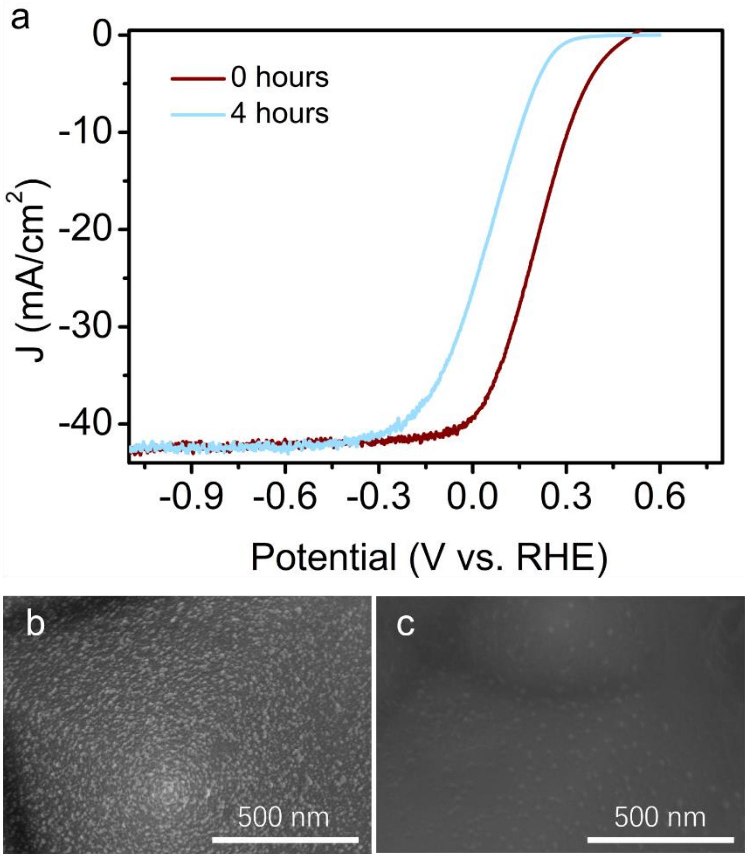

Figure S25. (a) Representative Ir/Ni/Si sample LSV curves collected periodically during 4 h of operation. (b) and (c) SEM images of the Ir/Ni/Si before after the 4h durability test.

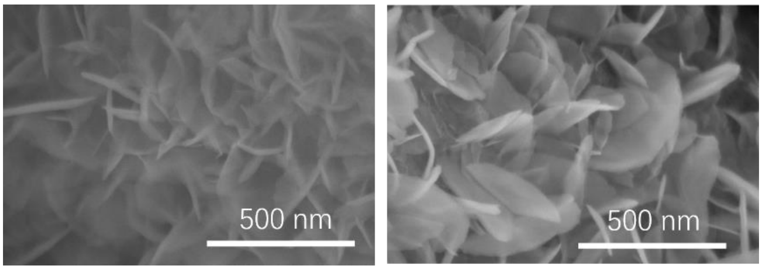

Figure S26. SEM images of the Ir/$Ni(OH)_2$/Ni/Si before and after the 170h durability test.

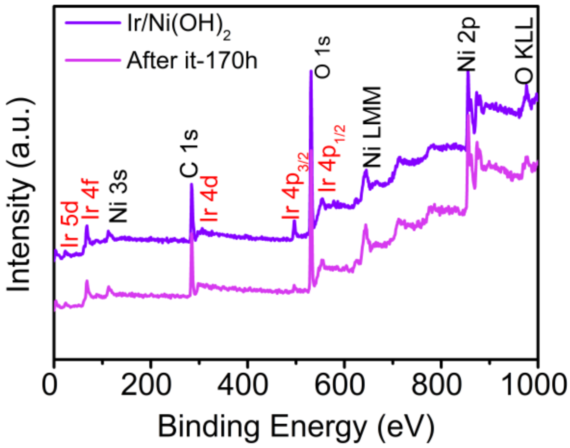

Figure S27. XPS survey spectra of the Ir/$Ni(OH)_2$/Ni/Si sample before and after 170 h durability test.

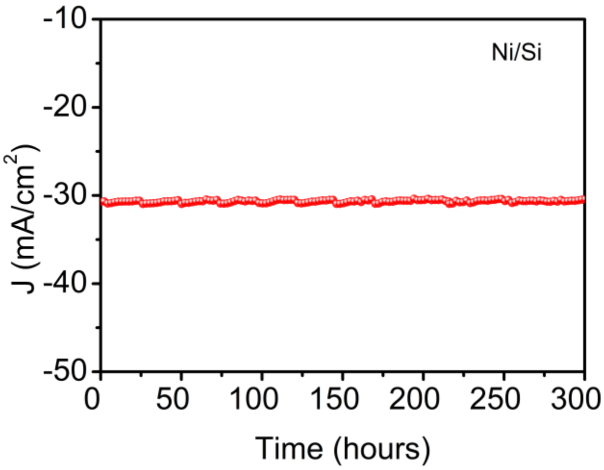

Figure S28. Chronoamperometic current versus time (j–t) curves of Ni/Si photocathode measured at 0 V_{RHE} under simulated AM 1.5G one sun illumination in 1 M KOH.

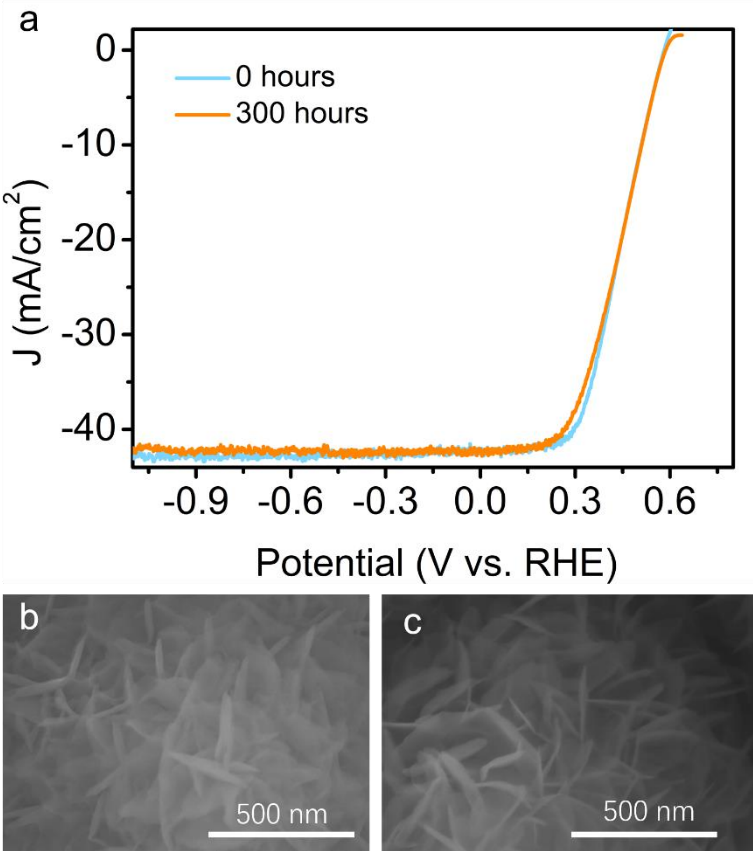

Figure S29. (a) Representative Ir/r-Ni(OH)$_2$/Ni/Si LSV curves collected periodically during 300 h of operation. (b) and (c) SEM images of the Ir/r-Ni(OH)$_2$/Ni/Si before and after the 300 h durability test.

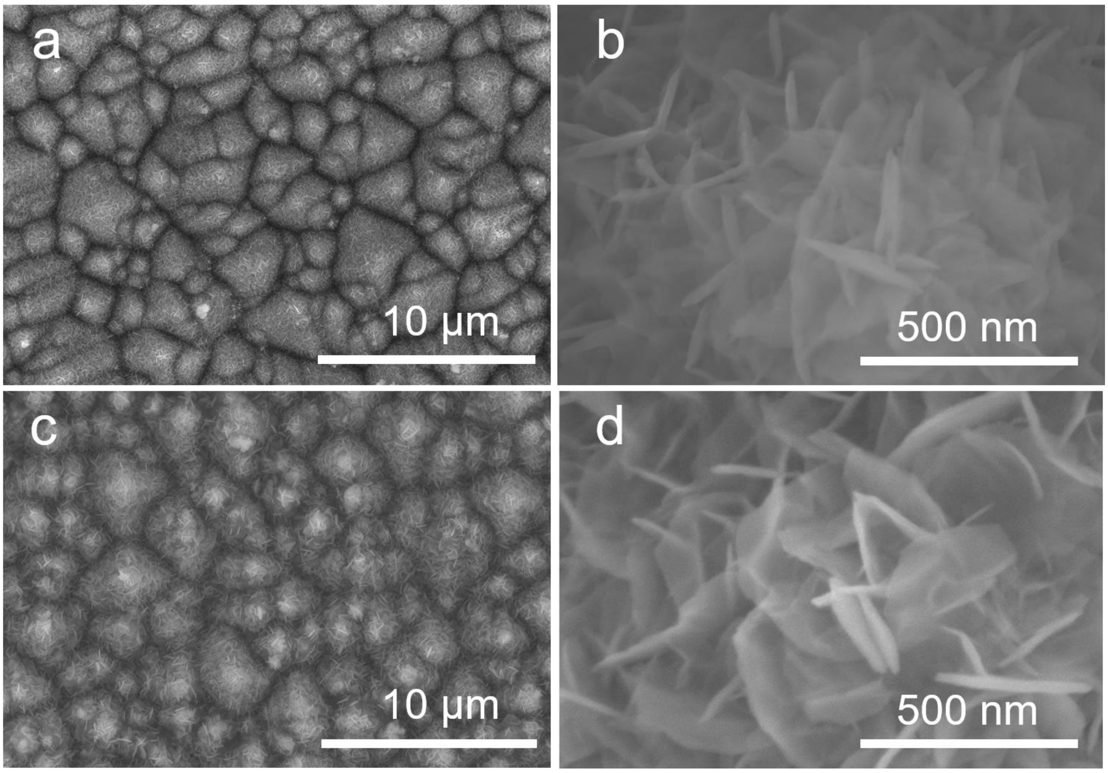

Figure S30. SEM images of $Ni(OH)_2/Ni/Si$ (a, b) before and (c, d) after the 300 h durability test.

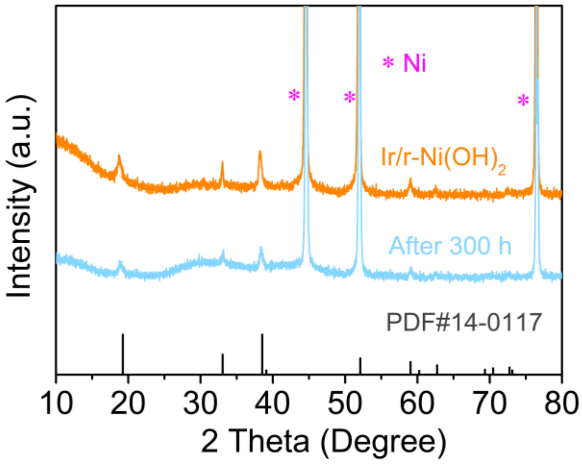

Figure S31. XRD patterns of the $Ir/r\text{-}Ni(OH)_2/Ni/Si$ before and after the 300 h durability test.

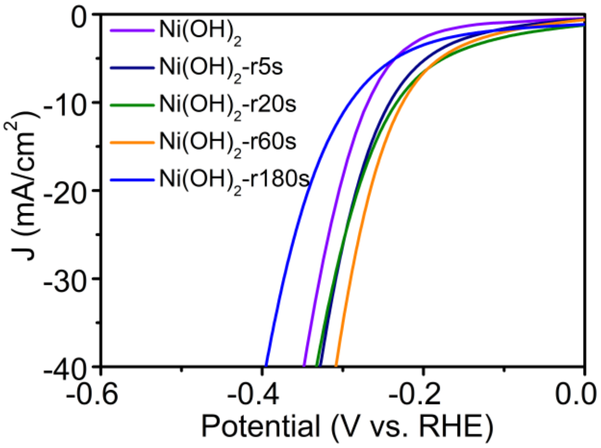

Figure S32. HER polarization curves of $Ni(OH)_2$ treated by $NaBH_4$ for different times.

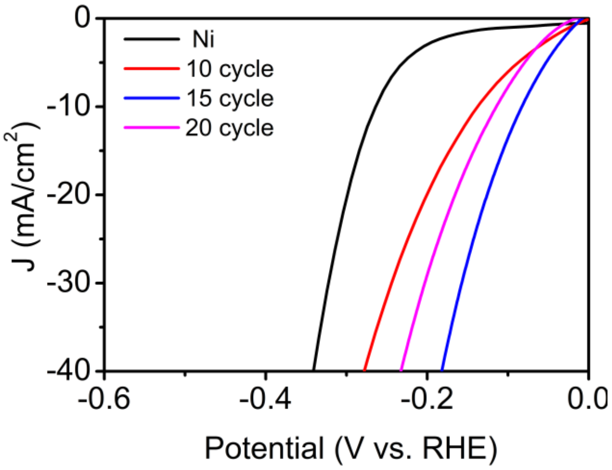

Figure S33. HER polarization curves of Ir catalyst with different loading amount on Ni.

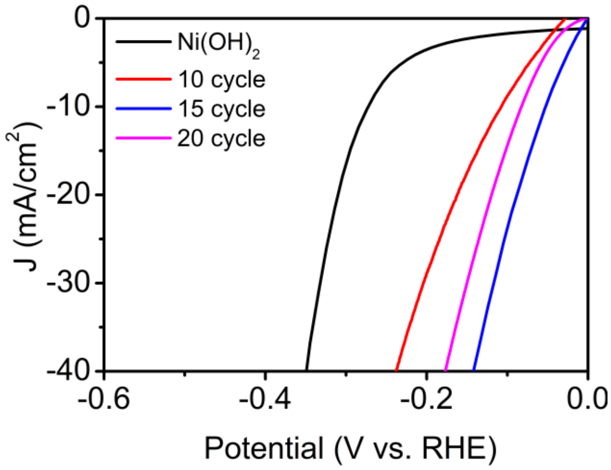

Figure S34. HER polarization curves of Ir catalyst with different loading amount on $Ni(OH)_2/Ni$.

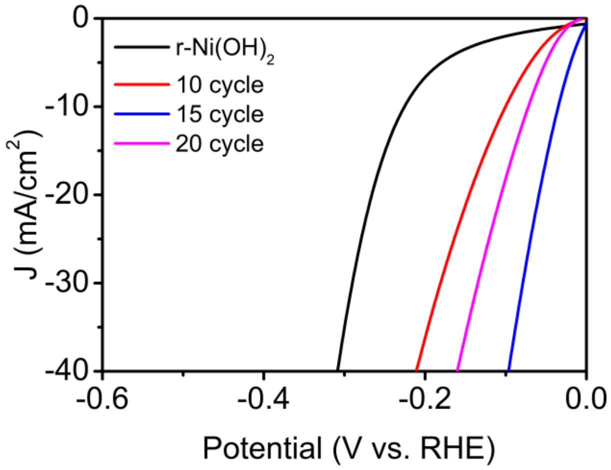

Figure S35. HER polarization curves of Ir catalyst with different loading amount on r-$Ni(OH)_2/Ni$.

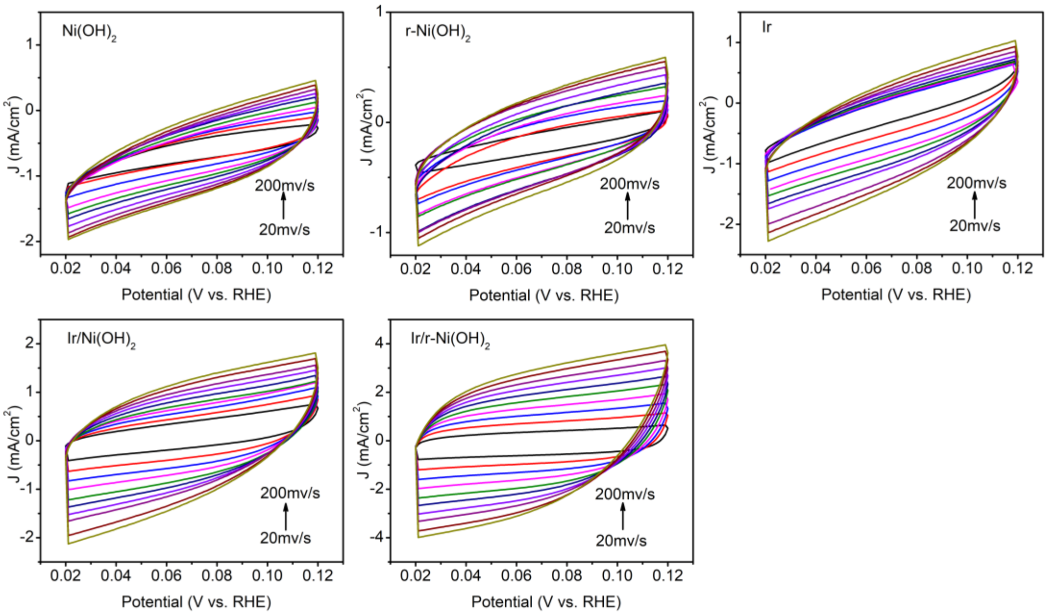

Figure S36. Cyclic voltammetry for HER at the scan rates of 20, 40, 60, 80, 100, 120, 140, 160, 180 and 200 mV/s in the range of no Faradaic processes for measuring the C_{dl} of $Ni(OH)_2$, r-$Ni(OH)_2$, Ir, Ir/$Ni(OH)_2$ and Ir/r-$Ni(OH)_2$ samples.

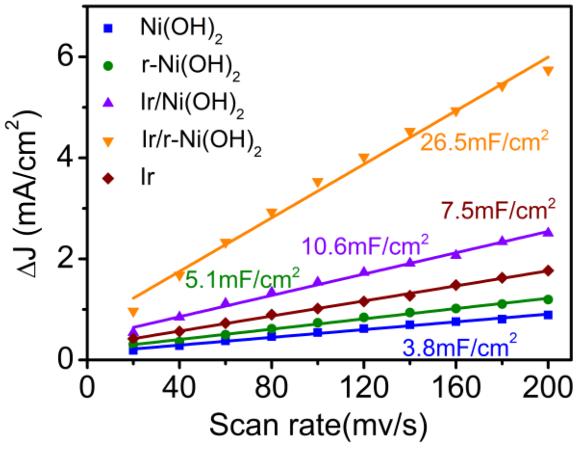

Figure S37. C_{dl} values estimated in HER.

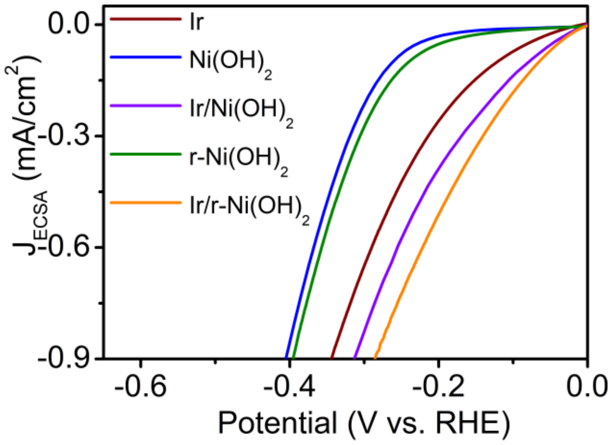

Figure S38. ECSA normalized LSV curves of various samples.

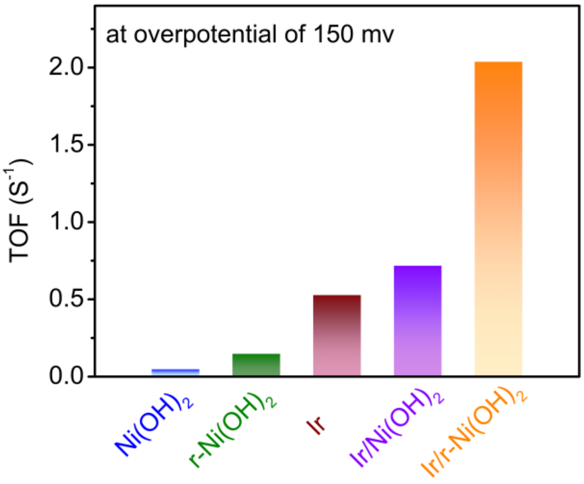

Figure S39. TOF calculation for HER at -0.15 V_{RHE} for various samples.

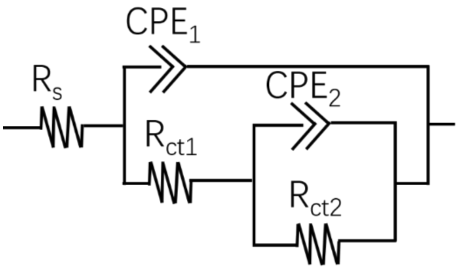

Figure S40. The equivalent circuit model corresponding to the charge transfer from the Si electrode to the electrolyte. The equivalent circuit elements include a series resistance (R_s) in series with two parallel arrangement of charge-transfer resistances (R_{ct}) and constant phase element (CPE).

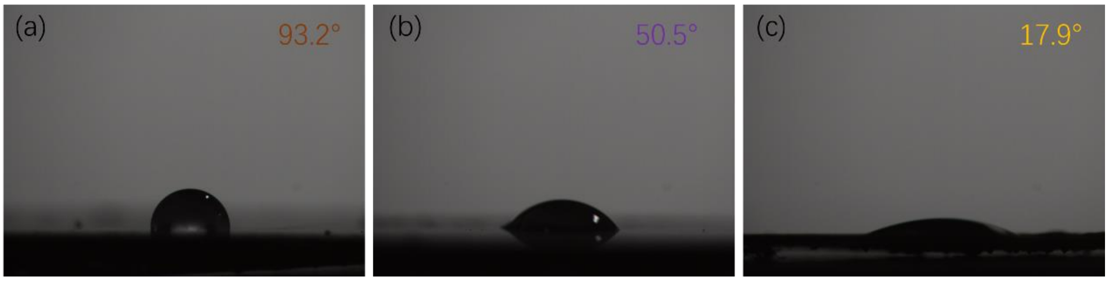

Figure S41. Static water contact angles for (a) Ir/Ni/Si, (b) Ir/Ni($OH)_2$/Ni/Si and (c) Ir/r-Ni($OH)_2$/Ni/Si samples in 1 M KOH under simulated AM1.5G one sun illumination.

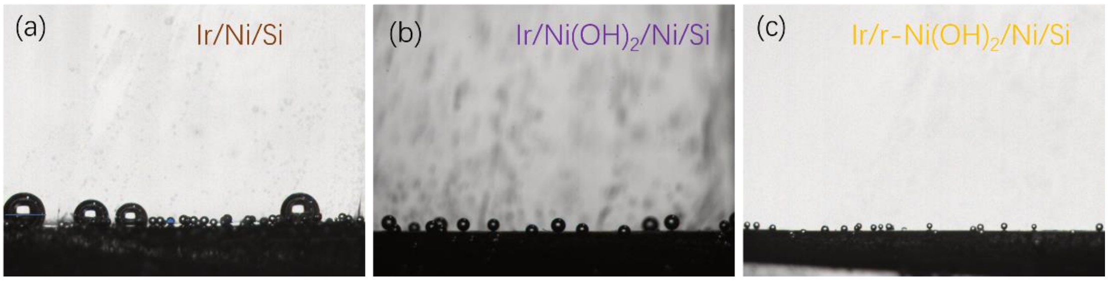

Figure S42. Digital photographs of hydrogen bubbles released at the surface of (a) Ir NPs/Ni/Si, (b) Ir/Ni($OH)_2$/Ni/Si, and (c) Ir/r-Ni($OH)_2$/Ni/Si samples at the same current density of −10mA/cm^2.

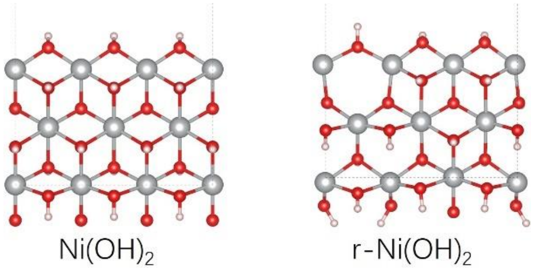

Figure S43. The as-built models for Ni($OH)_2$ and r-Ni($OH)_2$.

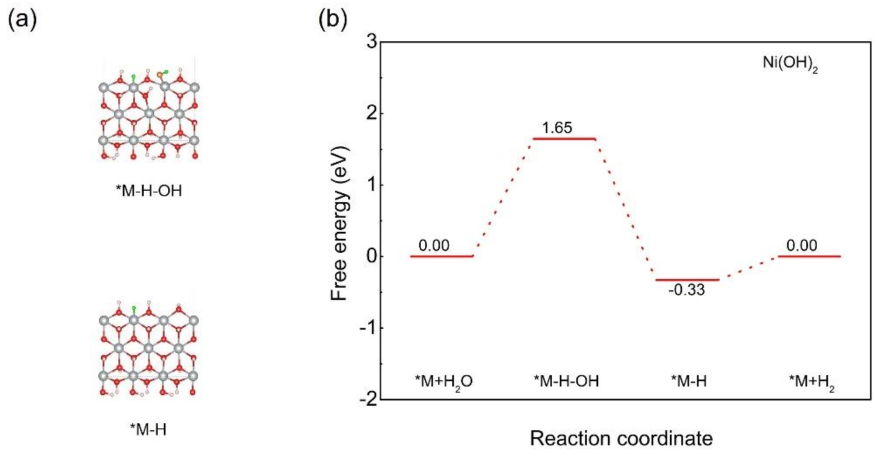

Figure S44. (a) The as-built structural models of the $Ni(OH)_2$ for different steps of HER and (b) the corresponding calculated Gibbs free energy diagrams for alkaline HER.

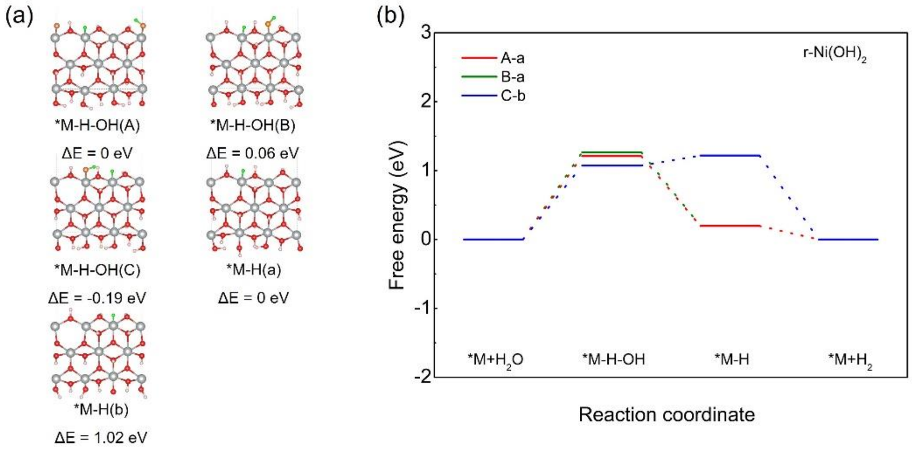

Figure S45. (a) The as-built structural models of the r-$Ni(OH)_2$ for different steps of HER and (b) the corresponding calculated Gibbs free energy diagrams for alkaline HER.

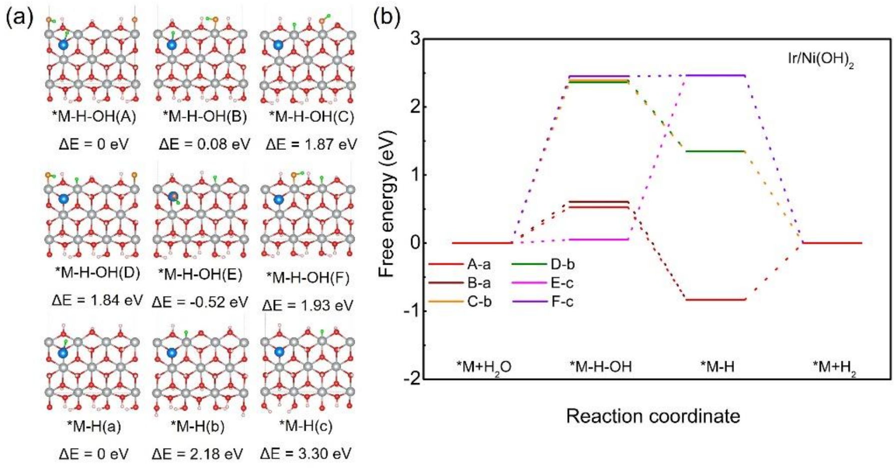

Figure S46. (a) The as-built structural models of the Ir/Ni(OH)$_2$ for different steps of HER and (b) the corresponding calculated Gibbs free energy diagrams for alkaline HER.

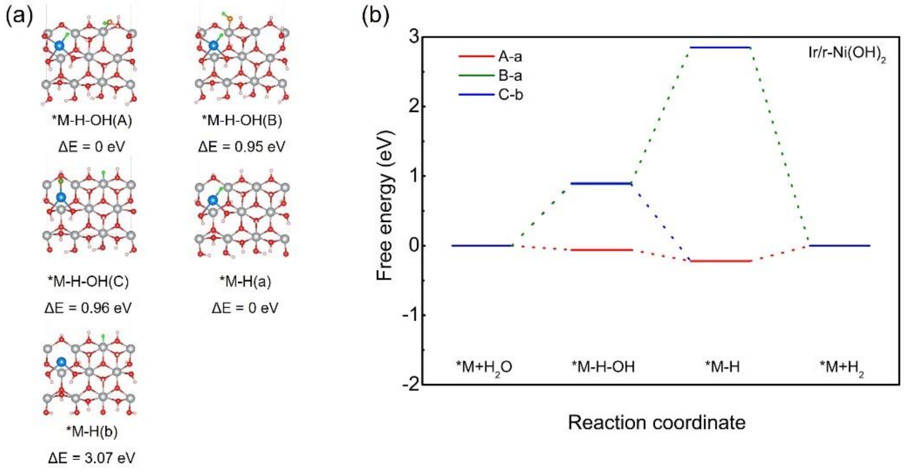

Figure S47. The as-built structural models of the Ir/r-Ni(OH)$_2$ for different steps of HER and (b) the corresponding calculated Gibbs free energy diagrams for alkaline HER.

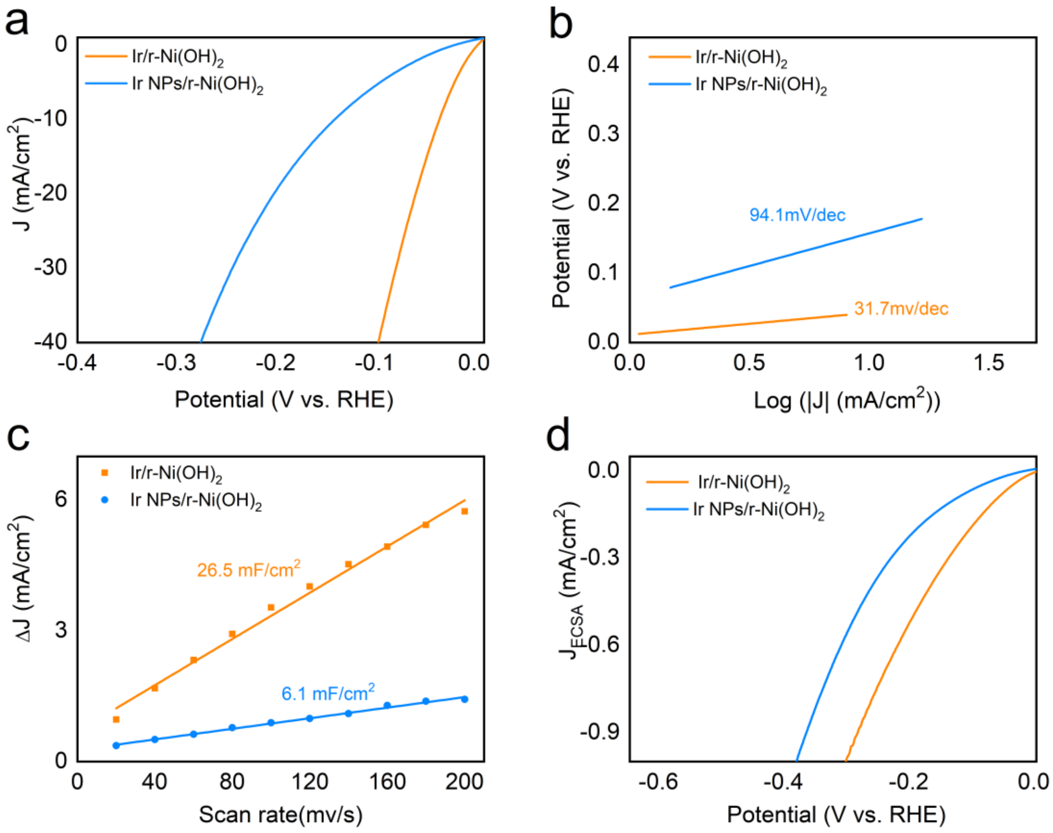

Figure S48. Electrocatalytic performance of the Ir/r-Ni(OH)2 and Ir NPs/r-Ni(OH)2. (a) LSV curves in 1 M KOH. (b) The corresponding Tafel plots derived from the LSV curves in (a). (c) Cdl values estimated in HER. (d) ECSA normalized LSV curves of various samples.

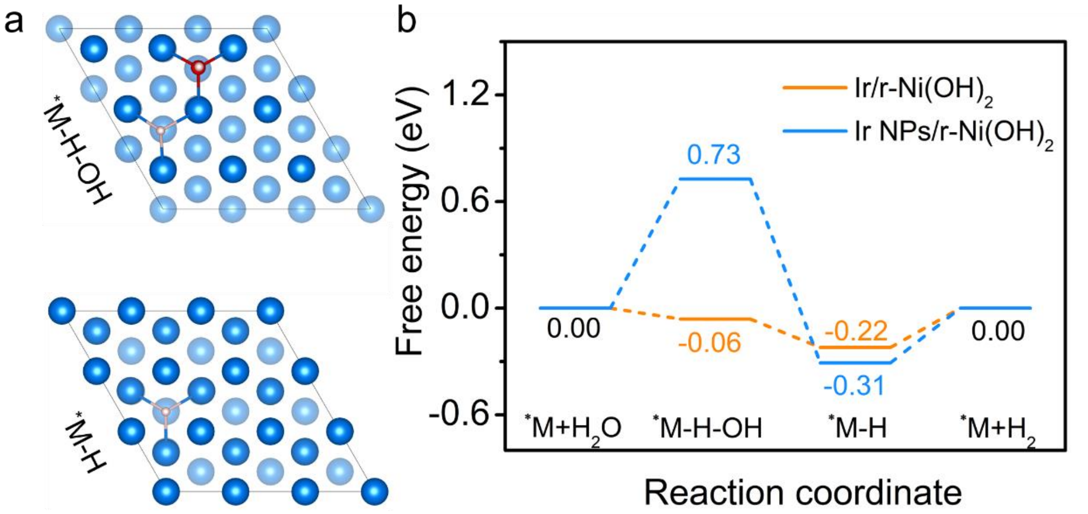

Figure S49. (a) The as-built structural models of the Ir NPs/r-$Ni(OH)_2$ for different steps of HER and (b) calculated Gibbs free energy diagrams for alkaline HER on Ir NPs/r-$Ni(OH)_2$ and Ir/r-$Ni(OH)_2$ surfaces.

Table S1. Content of Ir on the Ir/Ni/Si, Ir/Ni$(OH)_2$/Ni/Si and Ir/r-Ni$(OH)_2$/Ni/Si samples determined by ICP-AES.

Sample	**Ni (ppm)**	**Ir (ppm)**	**Atomic ratio of metals (Ni:Ir)**	**Ir content (wt%)**
Ir/Ni/Si	0.059	2.685	0.022:1	5.39±0.07
Ir/Ni$(OH)_2$/Ni/Si	261.8	1.165	224.7:1	2.33±0.08
Ir/r-Ni$(OH)_2$/Ni/Si	226.4	0.667	339.4:1	1.34±0.06

Table S2. The full width at half maxima (FWHM) of M−O, OVs and O_{abs} during the deconvolution of O 1s spectra for various samples.

Catalyst	**M−O (FWHM/eV)**	**OVs (FWHM/eV)**	**O_{abs} (FWHM/eV)**
Ni$(OH)_2$/Ni/Si	1.3	1.05	1.82
r-Ni$(OH)_2$/Ni/Si	1.05	1.3	1.9
Ir/Ni$(OH)_2$/Ni/Si	1.59	1.61	2
Ir/r-Ni$(OH)_2$/Ni/Si	1.59	1.58	2

Table S3. Convoluted peaks of O 1s and calculated oxygen vacancy concentration for various samples.

Catalyst	**M-O**	**OVs**	**O_{abs}**	**OVs/M-O ratio**
$Ni(OH)_2$/Ni/Si	51.4%	31.3%	17.3%	60.8%
r-$Ni(OH)_2$/Ni/Si	44.9%	37.2%	17.9%	82.8%
Ir/$Ni(OH)_2$/Ni/Si	53.3%	22.5%	24.2%	42.2%
Ir/r-$Ni(OH)_2$/Ni/Si	50.8%	29.4%	19.8%	57.8%

Table S4. Comparison of J_0, V_{on} and FF for various Si photocathodes.

Catalyst	**J_0 (mA/cm^2)**	**V_{on} (V_{RHE})**	**FF**
Ir/Ni/Si	-39.3	0.46	0.24
Ir/$Ni(OH)_2$/Ni/Si	-41.6	0.54	0.30
Ir/r-$Ni(OH)_2$/Ni/Si	-42.0	0.56	0.53

Table S5. Summary of PEC performance of state-of-the-art Si photocathodes.

Catalyst	**J_0 (mA/cm^2)**	**V_{on} (V_{RHE})**	**ABPE (%)**	**Stability (h)**	**Electrolyte**	**Ref.**
Ir/r-$Ni(OH)_2$/Ni/Si	-42.4	0.56	12.4	300	1 M KOH	This work
MoS_2/Ni_3S_2/Ni/Si	-41.54	0.54	11.23	172	1 M KOH	Nano Energy, 2020, 71, 104631.
Ni/TiO_2/a-Si/n-c-Si/a-Si/ITO/TiO_2/Pt	-35	0.62	12.66	108	1 M $HClO_4$	Energy Environ. Sci., 2020, 13, 221-228.
n^+p-Si/Ti/Ni	-38.7	0.61	5.1	8	1 M KOH	Inorg. Chem. Front., 2019,6, 527-532
Ni-Mo/Ni/n^+np^+-Si	36.3	0.50	6.9	100	1 M KOH	J. Mater. Chem. A, 2019,7, 2200-2209
Ni-Mo/NiSi/n^+p-Si microwires	-29.8	0.55	10.1	288	1 M KOH	ACS Energy Lett., 2018, 3, 1086-1092
Pd/TiO_2/b-Si	-8.3	0.32	< 0.5	2	1 M KOH	Nature Commun., 2018, 9, 3572
NiO_x/SiO_2/p-Si	-31	~0.8	3.1	1	1 M KOH	ACS Appl. Mater. Interfaces, 2018, 10, 7955-7962
NiFe LDH/Ti/p-Si	-7	~0.3	< 0.5	24	1 M KOH	ACS Energy Lett., 2017, 2, 1939-1946
Pt/TiO_2/F:SnO_2/Ti/n^+p-Si	35	0.5	10.9	24	1 M KOH	ACS Appl. Mater. Interfaces, 2014, 6, 22830-22837
TiO_2/Pt NPs/n^+np^+-Si	35.1	0.56	11.5	168	1 M $HClO_4$	Chem. Commun., 2018, 54, 543-546
Pt NPs/GaN nanowire/n^+-p-Si	38	0.5	10.5	113	0.5 M H_2SO_4	Nano Lett., 2018, 18, 6530-6537
MoS_x@GaN NWs/Si	40	0.4	5	10	0.5 M H_2SO_4	Nature Commun., 2018, 9, 3856

MoSe$_2$/n$^+$p-Si	29.3	0.4	3.8	120	1 M HClO$_4$	Appl. Phys. Lett., 2018, 112, 013902
Co-W-S/Ti/n$^+$p-Si	-30.4	0.36	4	144	1 M HClO$_4$	Appl. Catal. B: Environm., 2018, 237, 158-165
TiO$_2$/Pt NPs/n$^+$-p Si	35	0.54	10.8	168	1 M HClO$_4$	J. Mater. Chem. A, 2017, 5,18744-18751
MoS$_2$/Al$_2$O$_3$/n$^+$p-Si	35.6	0.4	3.6	120	1 M HClO$_4$	ACS Appl. Mater. Interfaces, 2017, 9, 6123-6129
Pt@SiO$_2$/pn$^+$-Si	30	0.49	8.9	22	K$_2$SO$_4$ and H$_2$SO$_4$	Appl. Phys. Lett., 2016, 109, 233901
MoS$_x$Cl$_y$/n$^+$pp$^+$-Si MPs	43	0.41	~6	2	0.5 M H$_2$SO$_4$	Adv. Mater., 2015, 27, 6511-6518
CoPS/n$^+$pp$^+$-Si MPs	26	0.42	4.7	-	0.5 M H$_2$SO$_4$	Nat. Mater., 2015, 14, 1245-1251
NiMo/TiO$_2$/n$^+$p-Si microwire	14.3	0.42	2.9	7	0.5 M H$_2$SO$_4$	Energy Environ. Sci., 2015, 8, 2977-2984
MoS$_2$/n$^+$p-Si	17	0.32	< 2	100	0.5 M H$_2$SO$_4$	Adv. Energy Mater., 2014, 1400739
MoQ$_x$Cl$_y$ /n$^+$pp$^+$ Si MP	43	0.41	-	2	0.5 M H$_2$SO$_4$	Adv. Mater., 2015,27(41), 6511-6518.

Table S6. Elemental atomic composition of the Ir/Ni(OH)$_2$/Ni/Si before and after 170 h test obtained from XPS survey scans.

Catalyst	**Ni（at%）**	**Ir（at%）**	**O（at%）**	**C（at%）**
Ir/Ni(OH)$_2$/Ni/Si before 170 h test	12.59%	2.25%	48.24%	36.92%
Ir/Ni(OH)$_2$/Ni/Si after 170 h test	12.39%	0.71%	47.48%	39.42%

Table S7. The fitted value of series resistance, charge transfer resistance and capacitance values for various catalysts on Ni/Si at 0.2 V$_{RHE}$ in 1 M KOH under AM 1.5G one sun illumination using the equivalent circuits listed in Figure 4a.

Catalyst	**Solution serious resistance (R_s) Ω**	**Change transfer resistance (R_{ct1}) Ω**	**Change transfer resistance (R_{ct2}) Ω**
Ir/Ni/Si	4.87	0.85	46.80
Ir/Ni(OH)$_2$/Ni/Si	4.62	1.11	23.18
Ir/r-Ni(OH)$_2$/Ni/Si	4.88	0.79	3.36

References:

1. Kresse and Furthmüller, *Physical review. B, Condensed matter*, 1996, **54 16**, 11169-11186.
2. G. Kresse and J. Furthmüller, *Computational Materials Science*, 1996, **6**, 15-50.
3. G. Kresse and D. Joubert, *Phys. Rev. B*, 1999, **59**, 1758.
4. J. P. Perdew, K. Burke and M. Ernzerhof, *Phys. Rev. Lett.*, 1996, **77**, 3865-3868.
5. J. K. Nørskov, J. Rossmeisl, A. Logadottir, L. Lindqvist, J. R. Kitchin, T. Bligaard and H. Jónsson, *The Journal of Physical Chemistry B*, 2004, **108**, 17886-17892.